

1 **Geostrophy assessment and momentum balance of the**
2 **global oceans in a tide- and eddy-resolving model**

3 **Xiaolong Yu¹, Aurélien L. Ponte¹, Noé Lahaye², Zoé Caspar-Cohen¹, Dimitris**
4 **Menemenlis³**

5 ¹Ifremer, Université de Brest, CNRS, IRD, Laboratoire d'Océanographie Physique et Spatiale (LOPS),

6 IUEM, Brest, France

7 ²Inria & IRMAR, campus universitaire de Beaulieu, Rennes, France

8 ³Jet Propulsion Laboratory, California Institute of Technology, Pasadena, California, USA

9 **Key Points:**

- 10 • We assess the accuracy of global geostrophy using instantaneous model fields.
11 • Geostrophic balance captures the leading-order dynamics in the ocean's major current
12 regions of high kinetic energy.
13 • The geostrophic imbalance of instantaneous fields is globally dominated by fast inter-
14 nal waves and turbulent stress divergence.

Corresponding author: Xiaolong Yu, xiaolong.yu@ifremer.fr

Abstract

Current satellite altimeters map sea surface height (SSH) with an effective spatial scale of $O(100 \text{ km})$ and, as a result, surface ocean velocity can be appropriately estimated from merged SSH fields by assuming geostrophic equilibrium. The validity of the geostrophic assumption down to the spatial scale of $O(10 \text{ km})$ that will be newly resolved by the next generation of satellite altimeters, such as the Surface Water Ocean Topography (SWOT) mission, remains unknown. In this study, the accuracy of geostrophy for the estimation of surface currents from a knowledge of instantaneous sea level is quantified using the hourly fields from a tide- and eddy-resolving global numerical simulation. Geostrophic balance is found to be the leading-order balance in frontal regions characterized by large kinetic energy, such as the western boundary currents and the Antarctic Circumpolar Current. Everywhere else, the ageostrophic flow is of comparable or larger amplitude than the total flow. As expected, the validity of geostrophy is shown to improve at low frequencies (typically $<0.5 \text{ cpd}$). Global estimates of the horizontal momentum budget reveal that the tropical and mid-latitude regions where geostrophic balance fails are dominated by fast (e.g., semidiurnal and supertidal) unbalanced motions and turbulent stress divergence terms rather than higher-order geostrophic terms. These findings indicate that the estimation of velocity from geostrophy applied on SWOT raw sea level maps may be challenging away from energetic areas.

Plain Language Summary

The geostrophic balance, which is a balance between the Coriolis force and the pressure gradient force, is a fundamental assumption that enables the estimation of the surface ocean circulation from SSH maps. The validity of this approximation down to spatial scales of order 10 km is critical to next-generation satellite altimetry missions, such as the upcoming Surface Water and Ocean Topography (SWOT) mission with a scheduled launch date in late 2022. In this study, we assess the degree of geostrophic validity using the instantaneous output from a high-resolution global model including tidal forcing. Our results suggest that geostrophic balance is a satisfactory approximation in energetic regions, such as the western boundary currents and the Antarctic Circumpolar Current. This is not the case however for the bulk of subtropical and subpolar open-ocean regions, suggesting that directly assuming geostrophy in these regions may lead to biased time-varying estimates of velocity. High-frequency signals dominate the ageostrophic motions everywhere except in the Southern Ocean, where the low-frequency wind-driven currents take over. These results suggest that using geostrophy on the raw maps of sea level collected by SWOT will not lead to an accurate prediction of surface currents away from energetic areas.

1 Introduction

About 80% of the kinetic energy in the ocean is contained at the mesoscale, where rotational effects are dominant and flows are approximately balanced and geostrophic (Ferrari & Wunsch, 2009). Mesoscale eddies in the ocean include coherent vortical structures with characteristic spatial scales of tens to hundreds of kilometers and temporal scales of weeks to months. Our understanding of mesoscale eddies dynamics has significantly advanced over the last 30 years owing to the availability of sea surface height (SSH) measurements that are routinely collected by satellite altimeters (Chelton et al., 2011; Morrow & Le Traon, 2012). The along-track SSH measurements from conventional nadir radar altimeters are typically merged and smoothed via objective analysis and optimal interpolation method to map SSH with uniform grid and global coverage. In doing so, gridded SSH maps typically resolve signals with horizontal and temporal resolutions of $O(100\text{ km})$ and $O(1\text{ month})$ (Ballarotta et al., 2019), and are widely used to infer the balanced flow field at the mesoscale and larger scales through the geostrophic approximation.

Submesoscale processes, characterized by smaller spatial scales of $O(1\text{-}10\text{ km})$ and shorter time scales (on the order of the local inertial period) than the mesoscale eddies, have come into focus more recently. Submesoscale motions are found to have an important contribution to vertical transport of buoyancy, nutrients and other biogeochemical tracers (see e.g., Lévy et al. (2018) for a review), and to transfer energy downscale from mesoscale eddies to small-scale turbulence (see e.g., McWilliams (2016) for a review). Dynamically, submesoscale processes are characterized by the Rossby number and bulk Richardson number on the order of unity, and thus are posited to be in partial geostrophic balance (Thomas et al., 2008). Submesoscale motions have been highlighted by a few very recent in situ observations to affect restratification of the upper ocean and to modulate the evolution of the mixed layer on climatic time scales (du Plessis et al., 2019; Siegelman et al., 2020; Yu et al., 2021). Numerical studies further indicate that high-frequency submesoscale motions, including unbalanced inertia-gravity waves, may contribute to the vertical global heat transport equally as the subinertial balanced component (e.g., Su et al., 2020). Thus, investigating the dominance of balanced and unbalanced motions at the submesoscale and specifically, the degree of geostrophic validity, is a fundamental requirement to gauge the relative contributions of the two components, and to fully understand their respective roles in shaping the ocean’s vertical transport and energy transfers (e.g., Schubert et al., 2020).

Investigations of geostrophic validity for instantaneous fields are motivated by the future wide-swath altimetry missions, such as the upcoming Surface Water and Ocean Topography (SWOT) altimeter mission (Morrow et al., 2019) and the Chinese ‘Guanlan’ mission which is in the early designing stage (Chen et al., 2019). With the advent of wide-swath radar interferometry, the SWOT mission is expected to measure, for the first time, the SSH globally and at spatial scales down to 15-50 km depending on the local sea state (Callies & Wu, 2019; J. Wang et al., 2019). For SWOT, the estimation of surface velocity from the operational SSH maps may still be founded on the geostrophic approximation. Besides the inherent measurement noise, critical challenges for the analysis SWOT data may also come from the long repeat cycle of SWOT orbit and the scale overlap between balanced motions and unbalanced inertia-gravity waves and their interactions (Ponte et al., 2017; Torres et al., 2018; Lahaye et al., 2019; Klein et al., 2019), which result in aliased variability associated with unbalanced motions in the SSH measurements. The inertia-gravity waves include internal waves and tides, near-inertial waves (NIWs) and internal wave continuum.

High-resolution ocean models that include astronomical tidal forcing provide a useful testbed to explore and unravel the issue of balance/unbalanced disentanglement in the SWOT mission. For instance, Qiu et al. (2018) indicated that the spatial transition length scale separating balanced geostrophic flows and unbalanced inertia-gravity waves on a global scale strongly depends on the energy level of local mesoscale eddy variability. Savage et al. (2017) provided global SSH variance associated with semidiurnal and diurnal tides and subtidal motions from a yearlong HYCOM output. The SSH signature of internal tides

103 and internal wave continuum may result in contamination in the SSH-derived velocity esti-
 104 mates directly through geostrophy at the resolution of SWOT, as illustrated by a regional
 105 simulation in Chelton et al. (2019).

106 Low-frequency wind-driven currents represent another important component of the
 107 ageostrophic motions at the surface. The classical paradigm of the wind-driven current
 108 is founded on Ekman theory (Ekman, 1905), which assumes a steady, linear and vertically
 109 homogeneous ocean on a large spatial scale. The current arises from the balance between
 110 the Coriolis force and the vertical convergence of the turbulent stress due to the winds
 111 (Lagerloef et al., 1999). In this view, the vertical structure of the Ekman currents is a spiral
 112 rotating clockwise (anticlockwise) with depth in the Northern (Southern) Hemisphere, with
 113 a surface current directed at 45° to the right (left) of the wind in the Northern (Southern)
 114 Hemisphere. Recent studies have extended this classical picture to time dependent config-
 115 urations (e.g., Shrira & Almelah, 2020). Efforts have been put into approximating global
 116 wind-driven currents from reanalysis surface wind fields in order to isolate them from the
 117 SSH-derived surface velocity (e.g., Rio, 2003). Satellite missions that are still under devel-
 118 opment, such as Winds and Currents Mission (WaCM; Rodriguez et al., 2018), the Surface
 119 Kinematic Monitoring (SKIM; Arduin et al., 2018) mission and Ocean Surface Current
 120 multiscale Observation Mission (OSCOM; Du et al., 2021), aim at measuring simultane-
 121 ously ocean surface winds and currents on a global scale using a Doppler scattermeter. The
 122 instantaneous current and wind measurements from these missions will allow a more direct
 123 estimation of geostrophic and Ekman currents globally.

124 In this study, we assess the accuracy of global geostrophy using instantaneous fields
 125 at hourly intervals from a tide- and eddy-resolving ocean simulation. We decompose the
 126 velocity field into two components: the geostrophic velocity computed from SSH derivatives
 127 in space directly from SSH rotated gradient, and the other ageostrophic velocity defined
 128 as the difference between the total velocity and the geostrophic one. We examine the
 129 kinetic energy levels of geostrophic and ageostrophic horizontal velocities geographically
 130 and spectrally, and finally explore the governed momentum balance underpinning. The
 131 paper is organized as follows. Section 2 introduces the simulation, the momentum balance
 132 framework, and methods of velocity decomposition and spectral analysis. Diagnostics about
 133 geostrophic accuracy are described in section 3 along with a more detailed investigation of
 134 surface momentum equilibriums. Discussions and conclusions are offered in sections 4 and
 135 5, respectively.

136 2 Materials and Methods

137 2.1 LLC4320 Simulation

138 The output from a state-of-the-art global numerical simulation, namely LLC4320 (Su
 139 et al., 2018), is employed to assess the validity of geostrophic approximation and horizontal
 140 momentum balances at the surface layer of the global oceans. The LLC4320 simulation
 141 was performed using the MITgcm (Marshall et al., 1997) on a global latitude-longitude-cap
 142 (LLC) grid (Forget et al., 2015) for a period of 14 months between 10 September 2011 and 15
 143 November 2012. The model has a horizontal grid spacing of $1/48^\circ$ (approximately 2.3 km at
 144 the equator and 0.75 km in the Southern Ocean), and thereby resolves mesoscale eddies and
 145 part of the internal wave field and permits submesoscale variability. Horizontal wavenumber
 146 spectra suggest that the effective horizontal resolution of LLC4320 is about 8 km (Rocha et
 147 al., 2016). The model time step was 25 seconds, and model variables were stored at hourly
 148 intervals. The model was forced at the surface by 6-hourly surface flux fields (including
 149 10-m wind velocity, 2-m air temperature and humidity, downwelling long- and short-wave
 150 radiation, and atmospheric pressure load) from the ECMWF operational reanalysis, and
 151 included the full luni-solar tidal constituents that are applied as additional atmospheric
 152 pressure forcing. The LLC4320 uses a flux-limited monotonicity-preserving (seventh order)
 153 advection scheme, and the modified Leith scheme of Fox-Kemper and Menemenlis (2008) for

154 horizontal viscosity. The K-profile parameterization (Large et al., 1994) is used for vertical
 155 viscosity and diffusivity. In this study, we use a yearlong record of the instantaneous surface
 156 fields at every hour, starting on 15 November 2011.

157 Physical processes captured by the simulation are illustrated with an SSH snapshot on
 158 24 November 2011 (Figure 1). It includes a large-scale circulation with embedded mesoscale
 159 meanders and eddies (e.g., in the Southern Ocean) and internal tides (e.g., east of the Luzon
 160 Strait). Coastal regions, defined here as the areas with seafloor depths shallower than 500
 161 m, are mainly influenced by barotropic tides. Coastal regions show distinct features (e.g.,
 162 periodic amplitudes of SSH and velocity; see Movie S1) to open ocean regions. Furthermore,
 163 polar regions (mostly located in the areas with latitudes higher than 60°) are covered by
 164 sea ice seasonally or all year round. In the following analysis, we exclude both coastal and
 165 ice-covered regions on the basis that they should deserve dedicated studies.

166 2.2 Vector-invariant momentum equation

167 The vector-invariant form of the momentum equation is employed for the LLC4320
 168 simulation,

$$\frac{\partial \vec{u}}{\partial t} + \underbrace{\vec{k}\zeta \times \vec{u} + \nabla \left(\frac{1}{2} \vec{u}^2 \right)}_{\vec{u} \cdot \nabla \vec{u}} + \underbrace{f \times \vec{u} + g \nabla \eta}_{f \times \vec{u}_a} = \vec{R}, \quad (1)$$

169 where $\vec{u} = (u, v)$ is the 2-d velocity vector, t is the time, \vec{k} is the vertical unit vector, ζ is
 170 the vertical component of relative vorticity, ∇ is the spatial gradient operator, $f = 2\Omega \sin \phi$
 171 is the Coriolis parameter (with Ω as Earth's angular velocity and ϕ as latitude), g is the
 172 gravitational acceleration, η is the SSH and \vec{R} is a residual term. The terms in the vector-
 173 invariant momentum equation are estimated using the hourly instantaneous output (i.e. off-
 174 line). The year-long time series of surface velocity and SSH fields are used to diagnostically
 175 estimate the terms of Equation (1).

176 The time acceleration term, $\frac{\partial \vec{u}}{\partial t}$, is calculated as a first-order derivative by a forward
 177 difference in time. The advection term, $\vec{u} \cdot \nabla \vec{u}$, is estimated as the sum of the nonlinear
 178 Coriolis term ($\vec{k}\zeta \times \vec{u}$) and the kinetic energy divergence term ($\nabla \left(\frac{1}{2} \vec{u}^2 \right)$). The sum of the
 179 linear Coriolis term ($f \times \vec{u}$) and the horizontal pressure gradient term ($g \nabla \eta$) yields $f \times \vec{u}_a$.
 180 This term represents the Coriolis force acting on the ageostrophic flow, and is referred to
 181 as the ageostrophic Coriolis term in this study. The residual term, \vec{R} , is estimated as the
 182 sum of the terms on the left-hand side of Equation (1). Note that \vec{R} includes the momen-
 183 tum contributions from turbulent stress divergence associated with atmospheric forcing and
 184 horizontal dissipation, sub-grid processes and all possible errors involved in the estimation
 185 process (e.g., discretization error associated with the hourly output sampling).

186 2.3 Geostrophic/ageostrophic decomposition

187 The geostrophic balance typically holds for ocean motions characterized by small Rossby
 188 number ($\text{Ro} \ll 1$) and low frequency (lower than the local inertial frequency) (Vallis, 2007).
 189 If these conditions are met, a balance exists between Coriolis and pressure gradient forces,

$$f \times \vec{u}_g = -g \nabla \eta, \quad (2)$$

190 where $\vec{u}_g = (u_g, v_g)$ is the geostrophic velocity vector. Thus, the time-varying horizontal
 191 velocity can be computed geostrophically from the instantaneous SSH field from the model
 192 output,

$$u_g = -\frac{g}{f} \frac{\partial \eta}{\partial y}, \quad v_g = \frac{g}{f} \frac{\partial \eta}{\partial x}. \quad (3)$$

193 Following Chelton et al. (2019), we refer to these estimates of geostrophic velocity (u_g, v_g) as
 194 geostrophically computed velocity. The potential limitations of velocity estimates from an
 195 instantaneous tide-resolving SSH map according to the geostrophic balance will be discussed

196 in section 4. The ageostrophic velocity (u_a, v_a) is defined as the difference between the total
 197 and geostrophically computed velocity,

$$u_a = u - u_g, v_a = v - v_g. \quad (4)$$

198 2.4 Frequency rotary spectrum

199 The yearlong time series of the surface horizontal velocity (u, v) , geostrophically com-
 200 puted velocity (u_g, v_g) and ageostrophic velocity (u_a, v_a) are respectively used to estimate
 201 their rotary spectra at model grid points. We first divide velocity time series into segments
 202 of 60 days overlapping by 50% and linearly detrend over each segment, and then compute
 203 the 1D discrete Fourier transform of complex-valued fields (e.g., $u + iv$) multiplied by a
 204 Hanning window. The spectra are formed by multiplying the Fourier coefficients by their
 205 complex conjugates, and the spectra are averaged over segments. We also integrate rotary
 206 frequency spectral densities over five frequency bands to compute kinetic energy components
 207 of interest, including high-frequency (>0.5 cpd, absolute values here and hereinafter), near-
 208 inertial ($0.9-1.1f$, absolute values here and hereinafter), semidiurnal ($1.9-2.1$ cpd), diurnal
 209 ($0.9-1.1$ cpd) and supertidal (>2.1 cpd). Our results are insensitive to the choice of the band
 210 limits (Yu et al., 2019). The kinetic energy components estimated from windowed spectra
 211 are then multiplied by a factor of $8/3$ to compensate for the Hanning windowing operation
 212 (Emery & Thomson, 2001). Total kinetic energy is estimated from temporal averages of
 213 instantaneous fields, and low-frequency kinetic energy is computed as total kinetic energy
 214 minus high-frequency kinetic energy.

215 3 Results

216 3.1 Surface kinetic energy distributions

217 The global snapshots of the zonal component of total velocity, geostrophically com-
 218 puted velocity and ageostrophic velocity are shown in Figure 2. At mid-latitudes ($30^\circ-60^\circ$
 219 N and S), the zonal velocity, u , compares visually well with the geostrophically computed
 220 velocity, u_g . This is especially true for the signature of energetic features, including the Gulf
 221 Stream, the Kuroshio Extension, the Brazil Current, the Agulhas Current and the Eastern
 222 Australian Current. The ageostrophic velocity, u_a , exhibits a spatial structure of $O(1000$
 223 km) superimposed with wave-like signals of $O(100$ km). A somewhat different picture is
 224 seen in the tropical and subtropical regions ($30^\circ\text{S}-30^\circ\text{N}$), where u reflects an alternating
 225 zonally elongated current system with typical amplitudes of the order to 1 m s^{-1} and vig-
 226 orous internal wave features such as in the southeast of the Luzon Strait. Both u_g and u_a
 227 exhibit, on the other hand, remarkably fine-scale wave-like structures associated with ampli-
 228 tudes greatly exceeding that of the full velocity field. These unrealistically large u_g and u_a
 229 mirror each other, and arise from the small-scale high-frequency variability in the SSH field
 230 (Figure S1) combined with reduced Coriolis parameter f near the equator. This highlights
 231 challenges for the estimation of surface velocity from future altimetric high-resolution SSH
 232 maps through geostrophic approximation at low latitudes. We exclude equatorial latitudes
 233 ($5^\circ\text{S}-5^\circ\text{N}$) in the following geostrophy assessment, but will explore the governing dynamics
 234 in the framework of momentum balance for the equatorial ocean in section 3.3.

235 The global distribution of the year-mean surface kinetic energy, KE , indicates that the
 236 ocean's kinetic energy is dominated by mesoscale-to-large-scale circulations in the regions of
 237 western boundary currents, the Antarctic Circumpolar Current (ACC) and the equatorial
 238 ocean (Figure 3). The magnitudes of kinetic energy in these energetic regions are on the
 239 order of $O(1$ m² s⁻²), exceeding typical values in the vast areas of other open-ocean regions
 240 (e.g., the eastern boundary current region of each ocean basin) by at least one order of mag-
 241 nitude. These modeled features of kinetic energy are broadly consistent with global drifter
 242 observations (Lumpkin & Johnson, 2013). In the energetic regions, patterns of kinetic energy
 243 resemble that associated with geostrophically computed velocity, KE_g , indicating that the

geostrophic component could explain much of the variance in these regions. By contrast, in other open-ocean regions (such as the mid-latitude South Pacific), the ageostrophic kinetic energy, KE_a , shows comparable energy levels with KE_g . As for snapshots, both KE_a and KE_g diverge in the equatorial oceans due to the vanishing Coriolis parameter. Lastly, there is no clear correspondence between KE_a and KE patterns, suggesting that higher-order geostrophic terms (e.g., cyclogeostrophic balance; Penven et al., 2014) may contribute only modestly to the ageostrophic circulation at a global scale.

The frequency rotary spectra of surface total velocity (\tilde{E}), geostrophically computed velocity (\tilde{E}_g) and ageostrophic velocity (\tilde{E}_a) as a function of latitude and frequency are shown in Figure 4. The velocity spectra are characterized by high-energy peaks at low frequencies (<0.5 cpd), diurnal, semidiurnal, and latitude-varying inertial frequencies. At low frequencies, the high-energy peaks of the surface total velocity field are reflected in geostrophic rotary spectra across all latitudes, whereas the ageostrophic rotary spectra peak more moderately. This translates the expected geostrophic balance holds at low frequencies. At high frequencies (>0.5 cpd), spectra estimated from geostrophically computed velocity and ageostrophic velocity exceed the total velocity spectra, especially at diurnal, semidiurnal and higher tidal harmonic frequencies. The cancellation between geostrophically computed and ageostrophic velocities indicates a failure of geostrophy at these frequencies. The energy peaks at the latitude-varying inertial frequencies are purely ageostrophic, due to the minor role played by pressure gradients for NIWs. The failure of geostrophy for tidal and near-inertial motions is not unexpected, because the inertia-gravity waves intrinsically relate to sea level according to polarization relations, which markedly depart from the geostrophic relation.

The low-frequency component of the geostrophically computed kinetic energy, $KE_{g,low}$, dominates that of the ageostrophic kinetic energy, $KE_{a,low}$, away from the equatorial band by a factor of 2-5, which highlights that the low-frequency total kinetic energy (which accounts for approximately 80% of the total kinetic energy globally), KE_{low} , is mainly composed of slow geostrophic motions (Figure 5a). The ageostrophic kinetic energy, KE_a , can be decomposed into components of different frequency bands using the spectra (Figure 5b). The low-frequency component, $KE_{a,low}$, tends to contribute increasingly to KE_a from low to high latitudes, and accounts for over 60% of KE_a in the Southern Ocean. Interestingly, supertidal motions are the dominant contributor to KE_a in the internal wave field, especially in tropical latitudes (also see Figure S2). Semidiurnal tides are the second largest component with the ratio $KE_{a,semi}/KE_a$ between 10% to 30% across latitudes. In contrast, NIWs and diurnal tides make only a modest contribution to the ageostrophic kinetic energy, up to 10%.

3.2 Geostrophy assessment

The ratio of ageostrophic kinetic energy to total kinetic energy, KE_a/KE , is used as a quantification of geostrophic validity (Figure 6). A threshold of ratio 0.2 is chosen arbitrarily here. The global map of KE_a/KE illustrates the dominant geostrophic character of the velocity field in the regions of energetic kinetic energy, primarily in the western boundary currents and the ACC in the subpolar region. The ratio KE_a/KE is commonly smaller than 0.2 there, which means that geostrophic motions account for more than 80% of the total kinetic energy. On the other hand, ageostrophic motions exhibit comparable or larger levels of kinetic energy than the total kinetic energy in most of the open-ocean regions (including the Canary Current, Benguela Current, the California Current and Peru Current), indicating that the geostrophic approximation is not a good estimator of the surface circulation with instantaneous fields there. For low-frequency motions, the ratio $KE_{a,low}/KE_{low}$ is significantly reduced globally away from the equatorial ocean. In the zonal average, the ratio KE_a/KE reaches its minimum of approximately 30% in the Southern Ocean, and down to below 50% at latitudes of the Kuroshio and the Gulf Stream (30° - 40° N). Zonally-averaged $KE_{a,low}/KE_{low}$ is always lower than that of KE_a/KE , with a range of 10% to

296 60% at extratropical latitudes. Particularly, the ratio $KE_{a,low}/KE_{low}$ decreases to 20% in
 297 the Southern Ocean and to 10% in the 30°-40°N band.

298 In order to gain deeper insight into the temporal scale of the validity of geostrophic
 299 balance, the ratio of the rotary frequency spectra of ageostrophic velocity to total velocity
 300 (\tilde{E}_a/\tilde{E}) is computed (Figure 7). Across all latitudes, super-inertial (i.e., frequencies exceed-
 301 ing f) motions are dominated by ageostrophic dynamics. There is an obvious asymmetry
 302 between cyclonic and anticyclonic motions within the subinertial band (i.e., frequencies
 303 lower than f), where cyclonic motions appear to be more geostrophic at higher frequencies.
 304 For instance, the frequency scale for the validity of geostrophy under a 0.2 ratio threshold
 305 is approximately 0.15 cpd (i.e. 6.7 days) for cyclonic motions and 0.05 cpd (i.e. 20 days)
 306 for anticyclonic motions at latitudes of the Kuroshio and the Gulf Stream (30°-40°N). This
 307 asymmetry is possibly due to the strongly polarized signature of NIWs extending down to
 308 lower frequencies under the influence of mesoscale eddies. The stronger influence of NIWs
 309 combined with their purely ageostrophic character would result in anticyclonic motions less
 310 geostrophic than cyclonic ones. Overall, the surface flows at frequencies less than approx-
 311 imately 0.05 cpd (i.e. periods longer than 20 days) follow the geostrophy balance (\tilde{E}_a/\tilde{E}
 312 ~ 0.2) to a first order, except in the quiescent subpolar region of the Northern Hemisphere
 313 and in the equatorial region where geostrophy does not hold due to the vanishing Coriolis
 314 parameter. This illustrates the expected result that the majority of large-scale gyres in the
 315 global oceans are in geostrophic balance at low frequencies.

316 3.3 Momentum balance

317 In order to identify more specifically sources of ageostrophic variability, we compute
 318 the annual root mean square (denoted as $\langle \cdot \rangle_{rms}$) of each term in Equation (1).

319 The global distributions of the root-mean-square values of the linear Coriolis and pres-
 320 sure gradient forces are displayed in Figure 8. Consistent with the regions of small KE_a/KE
 321 ratios (Figure 6a), both two terms show enhanced values in energetic regions (e.g., the South-
 322 ern Ocean and western boundary current system and extensions). One significant difference
 323 between the two terms is that the pressure gradient term also exhibits intense beam-like
 324 structures in the tropical region, whereas the linear Coriolis term is largely muted due to
 325 vanishing f . These beams emanate from known energetic internal tide generation sites (e.g.,
 326 Amazon plateau and West of Luzon strait), which suggests that they are the signature of
 327 propagating internal tides. The signature of these beams is also present on the root mean
 328 square of the acceleration term, albeit with a weaker amplitude, and on the residual term
 329 (Figure 9). Internal tides of large amplitudes may be associated with significant advection
 330 of momentum and/or may evolve rapidly compared to the model output frequency, which
 331 would both explain their signature on the residual. The advection term is only profound
 332 in regions of energetic kinetic energy, and shows qualitatively similar patterns to the linear
 333 Coriolis term but with a magnitude a factor of 2-5 smaller.

334 The zonally averaged root-mean-square values of the horizontal pressure gradient term
 335 are comparable in magnitude with those of the linear Coriolis term at mid-latitudes (Figure
 336 10a). The amplitude of ageostrophic Coriolis term ($\langle f \times \vec{u}_a \rangle_{rms}$) closely follows the pressure
 337 gradient one between 0°-30° N and S, where the value of the linear Coriolis term decreases
 338 with decreasing latitudes. The root mean square of the momentum balance residual covaries
 339 with $\langle f \times \vec{u}_a \rangle_{rms}$, albeit with a smaller amplitude (Figure 10b). The time acceleration term
 340 also broadly follows the latitudinal structure of $\langle f \times \vec{u}_a \rangle_{rms}$, and tend to have an increasing
 341 contribution momentum at low latitudes. Comparison of the ratio of each term to $\langle f \times$
 342 $\vec{u}_a \rangle_{rms}$ in Figure 11 shows that the acceleration and residual have comparable amplitudes
 343 with $\langle f \times \vec{u}_a \rangle_{rms}$ in the tropical region, which suggest a necessary cancellation between
 344 both terms. We have argued that the residual may be explained at the equator by the
 345 signature of large internal tides. At mid-latitudes, the residual term dominates $\langle f \times \vec{u}_a \rangle_{rms}$
 346 and we speculate this residual is dominated by vertical stress divergence associated with

347 winds. This is suggested by the lower frequency content of the residual (Figure S3) and
 348 its geographical distribution (Figure 11c). Finally, the advection term has a moderate
 349 contribution to $\langle f \times \vec{u}_a \rangle_{rms}$ over the global oceans, approximately 10% in the subtropical
 350 regions and up to 30% in the subpolar regions.

351 4 Discussion

352 In the previous section, the global validity of geostrophy using the instantaneous model
 353 fields was shown to be latitude- and frequency-dependent. We now discuss possible biases
 354 and limitations from our model study.

355 The LLC4320 simulation exhibits variance 4 times higher in the semidiurnal band and
 356 3 times lower in the inertial band compared with surface drifter data (Yu et al., 2019).
 357 The overly energetic semidiurnal tides, which are ubiquitous over the global oceans, would
 358 overestimate ageostrophic kinetic energy levels and thus lead to an underestimate of the
 359 degree of geostrophy validity. On the other hand, the deficit of the modeled near-inertial
 360 kinetic energy (which is purely ageostrophic) would lead to an optimistic geostrophy assess-
 361 ment. Note that the overly strong semidiurnal tides and too weak NIWs in LLC4320 may
 362 compensate one another in the estimate of ageostrophic kinetic energy.

363 The accuracy of geostrophic predictions of instantaneous sea level maps will be quan-
 364 titatively improved from a simulation with more realistic levels of the unbalanced inertia-
 365 gravity waves. Numerically, an increase of spatial and temporal resolutions of wind forcing
 366 is a key step to improving the near-inertial kinetic energy levels (Rimac et al., 2013; Flexas
 367 et al., 2019). The magnitude of internal tides is found to be sensitive to model damping
 368 parameterizations, such as a parameterized topographic internal wave drag which is not
 369 included in MITgcm (Arbic et al., 2018). For LLC4320, there is also some speculation that
 370 the overly large semidiurnal tides may be partially caused by mistakes in the implementa-
 371 tion of the ocean self-attraction and loading. Furthermore, Nelson et al. (2020) suggested
 372 that increasing the model horizontal resolution improves the comparison of modeled internal
 373 wave continuum with observations.

374 Practically speaking, the contamination of NIWs will be a greater challenge for near-
 375 nadir Doppler radar missions such as SKIM than for satellite altimetry missions such as
 376 SWOT (see Figure S1 as an illustration that NIWs have almost no signature on the SSH
 377 field). Another challenge is that instrumental noise levels inevitably prevent the analysis
 378 of raw sea level maps provided by SWOT and an averaging may be required (Chelton et
 379 al., 2019). A temporal average could also smooth both instrumental noise and the high-
 380 frequency variability that affects the accuracy of geostrophic currents for the estimation of
 381 surface currents. Time-averaged fields may be constructed either from repeated measure-
 382 ment swaths or from combing multiple satellite measurements. Moreover, one may speculate
 383 on the potential of having simultaneously maps of sea level (from SWOT) and surface cur-
 384 rents (from SKIM) to improve our understanding of high-frequency motions (e.g., one could
 385 directly compute observed ageostrophic currents via the combination of the two).

386 The horizontal and vertical components of turbulent stress divergence was unfortunately
 387 not available from the LLC4320 output for this study, and are included in the momentum
 388 residual here. At the ocean surface, the turbulent stress divergence is typically dominated
 389 by the frictional stress driven by wind forcing, and may be approximated from wind stress.
 390 We estimate this vertical divergence of wind stress term using a scaling approximate of
 391 $\vec{F}_v \approx \frac{1}{\rho_0} \frac{\vec{\tau}}{\delta_e}$, where \vec{F}_v is the vertical component of the turbulent stress divergence, ρ_0 is the
 392 reference density, $\vec{\tau}$ is the surface wind stress, $\delta_e = \gamma u_* / f$ is the Ekman layer depth with $u_* =$
 393 $\sqrt{|\vec{\tau}| / \rho_0}$ and $\gamma = 0.25$ is an empirical constant determined from observations (W. Wang &
 394 Huang, 2004). The results indicate that the vertical divergence of wind stress term displays
 395 moderate large-scale structures at mid-latitudes and could explain much of the variance
 396 of the residual term there (not shown). In the tropical latitudes, however, the residual

397 term is dominated by supertidal motions (Figure S3), and one could speculate that the
 398 turbulent stress divergence associated with horizontal dissipation might also be responsible.
 399 Another limitation is that the LLC4320 simulation was stored as hourly snapshots, and
 400 thus the velocity and SSH fields alias variability higher than the model output frequency. To
 401 examine the impact of the turbulent stress divergence and higher-frequency (i.e., subhourly)
 402 variability, an online (i.e., during model run time) momentum budget analysis would be more
 403 adequate; a regional simulation in the tropical region forced by the LLC4320 boundary
 404 conditions will be considered in future work.

405 5 Summary

406 Geostrophy is a fundamental approximation that has been widely applied to the present
 407 altimetric SSH measurements on scales of a few hundreds of kilometers. In this study, we
 408 assess the global validity of geostrophy down to the spatial scale of $O(10\text{ km})$, using the
 409 hourly instantaneous surface fields from the tide- and eddy-resolving LLC4320 simulation.
 410 The degree of geostrophic validity at this scale is particularly relevant to the usage of
 411 measurements from the upcoming SWOT mission. Our main conclusions are summarized
 412 as follows:

413 1. Geostrophic balance is the leading-order balance in the regions of energetic kinetic
 414 energy, such as the western boundary currents and the ACC. In contrast, for the bulk
 415 of other open ocean regions, such as the eastern boundary currents and the interior of
 416 subtropical and subpolar gyres, ageostrophic motions are at least comparable in magnitude
 417 to total motions in the context of kinetic energy levels, indicating geostrophy may not lead
 418 to accurate estimates of surface currents there if directly applied to SWOT raw sea level
 419 maps. In the equatorial ocean, geostrophy does not hold due to the Coriolis parameter
 420 approaching zero.

421 2. The accuracy of geostrophy for the estimation of surface currents is frequency-
 422 dependent. Low-frequency component of the surface flows tends to follow the geostrophic
 423 balance to a first order almost across the global oceans away from the equator. The range of
 424 validity of geostrophy extends down to time scales of 20 days in the subtropical and subpolar
 425 oceans.

426 3. Surface ageostrophic motions are dominated by supertidal motions and localized in-
 427 ternal tide motions within tropical latitudes. The relative contribution of supertidal motions
 428 decreases towards higher latitudes such that internal tides and low-frequency contributions
 429 (associated with winds and advection) become dominant. Low-frequency Ekman flows are
 430 found to have an increasing contribution at higher latitudes.

431 Our findings point out that the limitation of geostrophy will prevent the direct esti-
 432 mation of surface currents from SWOT maps. In order to provide accurate surface current
 433 estimates, it will be necessary, away from energetic areas, either to identify and subtract
 434 high-frequency motions (including internal tides and internal wave continuum), or to low-
 435 pass filter SSH measurements temporally. Given the importance of high-frequency motions
 436 in determining ageostrophic levels, there is also an opportunity that surface drifters repre-
 437 sent to better estimate high-frequency variability and to improve our expectations about
 438 the errors that will be made when applying geostrophy instantaneously (Elipot et al., 2016).

439 Acknowledgments

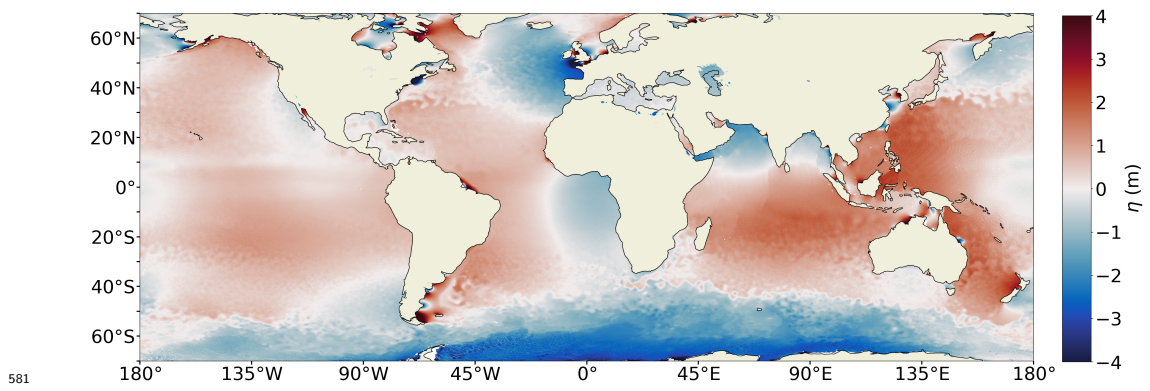
440 This work was carried out as part of the ANR project number 17-CE01-0006-01 and entitled
 441 EQUINOx (Disentangling Quasi-geostrophic Motions and Internal Waves in High Resolution
 442 Satellite Observations of the Ocean). It is also part of the CNES-TOSCA project entitled
 443 “New Dynamical Tools for submesoscale characterization in SWOT data” that was proposed
 444 within the context of the SWOT mission. The LLC output is available from the ECCO
 445 project (http://ecco2.org/llc_hires).

References

- Arbic, B., Alford, M. H., Ansong, J. K., Buijsman, M. C., Ciotti, R. B., Farrar, J. T., . . . Zhao, Z. (2018). A primer on global internal tide and internal gravity wave continuum modeling in hycom and mitgcm. *New Frontiers in Operational Oceanography*, E. P. Chassignet et al., Eds., *GODAE OceanView*, 307-392.
- Ardhuin, F., Aksenov, Y., Benetazzo, A., Bertino, L., Brandt, P., Caubet, E., . . . Xie, J. P. (2018). Measuring currents, ice drift, and waves from space: the sea surface kinematics multiscale monitoring (skim) concept. *Ocean Science*, *14*(3), 337-354.
- Ballarotta, M., Ubelmann, C., Pujol, M.-I., Taburet, G., Fournier, F., Legeais, J.-F., . . . Picot, N. (2019). On the resolutions of ocean altimetry maps. *Ocean Science*, *15*(4), 1091-1109.
- Callies, J., & Wu, W. (2019). Some Expectations for Submesoscale Sea Surface Height Variance Spectra. *Journal of Physical Oceanography*, *49*(9), 2271-2289.
- Chelton, D. B., Schlax, M. G., & Samelson, R. M. (2011). Global observations of nonlinear mesoscale eddies. *Progress in Oceanography*, *91*(2), 167-216.
- Chelton, D. B., Schlax, M. G., Samelson, R. M., Farrar, J. T., Molemaker, M. J., McWilliams, J. C., & Gula, J. (2019). Prospects for future satellite estimation of small-scale variability of ocean surface velocity and vorticity. *Progress in Oceanography*, *173*, 256-350.
- Chen, G., Tang, J., Zhao, C., Wu, S., Yu, F., Ma, C., . . . Wu, L. (2019). Concept design of the “guanlan” science mission: China’s novel contribution to space oceanography. *Frontiers in Marine Science*, *6*, 194.
- Du, Y., Dong, X., Jiang, X., Zhang, Y., Zhu, D., Sun, Q., . . . Peng, S. (2021). Ocean surface current multiscale observation mission (OSCOM): Simultaneous measurement of ocean surface current, vector wind, and temperature. *Progress in Oceanography*, *193*, 102531.
- du Plessis, M., Swart, S., Ansong, I. J., Mahadevan, A., & Thompson, A. F. (2019). Southern ocean seasonal restratification delayed by submesoscale wind-front interactions. *Journal of Physical Oceanography*, *49*(4), 1035-1053.
- Ekman, V. W. (1905). On the influence of the earth’s rotation on ocean currents. *Arkiv För Matematik, Astronomi Och Fysik*, *2*, 1-53.
- Elipot, S., Lumpkin, R., Perez, R. C., Lilly, J. M., Early, J. J., & Sykulski, A. M. (2016). A global surface drifter data set at hourly resolution. *Journal of Geophysical Research-Oceans*, *121*(5), 2937-2966.
- Emery, W. J., & Thomson, R. E. (2001). Chapter 5 - time-series analysis methods. In *Data analysis methods in physical oceanography* (p. 371-567).
- Ferrari, R., & Wunsch, C. (2009). Ocean circulation kinetic energy: Reservoirs, sources, and sinks. *Annual Review of Fluid Mechanics*, *41*, 253-282.
- Flexas, M. M., Thompson, A. F., Torres, H. S., Klein, P., Farrar, J. T., Zhang, H., & Menemenlis, D. (2019). Global estimates of the energy transfer from the wind to the ocean, with emphasis on near-inertial oscillations. *Journal of Geophysical Research-Oceans*, *124*(8), 5723-5746.
- Forget, G., Campin, J. M., Heimbach, P., Hill, C. N., Ponte, R. M., & Wunsch, C. (2015). Ecco version 4: an integrated framework for non-linear inverse modeling and global ocean state estimation. *Geoscientific Model Development*, *8*(10), 3071-3104.
- Fox-Kemper, B., & Menemenlis, D. (2008). Can large eddy simulation techniques improve mesoscale rich ocean models? In *Ocean modeling in an eddying regime* (p. 319-337). American Geophysical Union (AGU).
- Klein, P., Lapeyre, G., Siegelman, L., Qiu, B., Fu, L.-L., Torres, H., . . . Le Gentil, S. (2019). Ocean-scale interactions from space. *Earth and Space Science*, *6*(5), 795-817.
- Lagerloef, G. S. E., Mitchum, G. T., Lukas, R. B., & Niiler, P. P. (1999). Tropical pacific near-surface currents estimated from altimeter, wind, and drifter data. *Journal of Geophysical Research: Oceans*, *104*(C10), 23313-23326.
- Lahaye, N., Gula, J., & Roulet, G. (2019). Sea surface signature of internal tides. *Geophysical Research Letters*, *46*(7), 3880-3890.

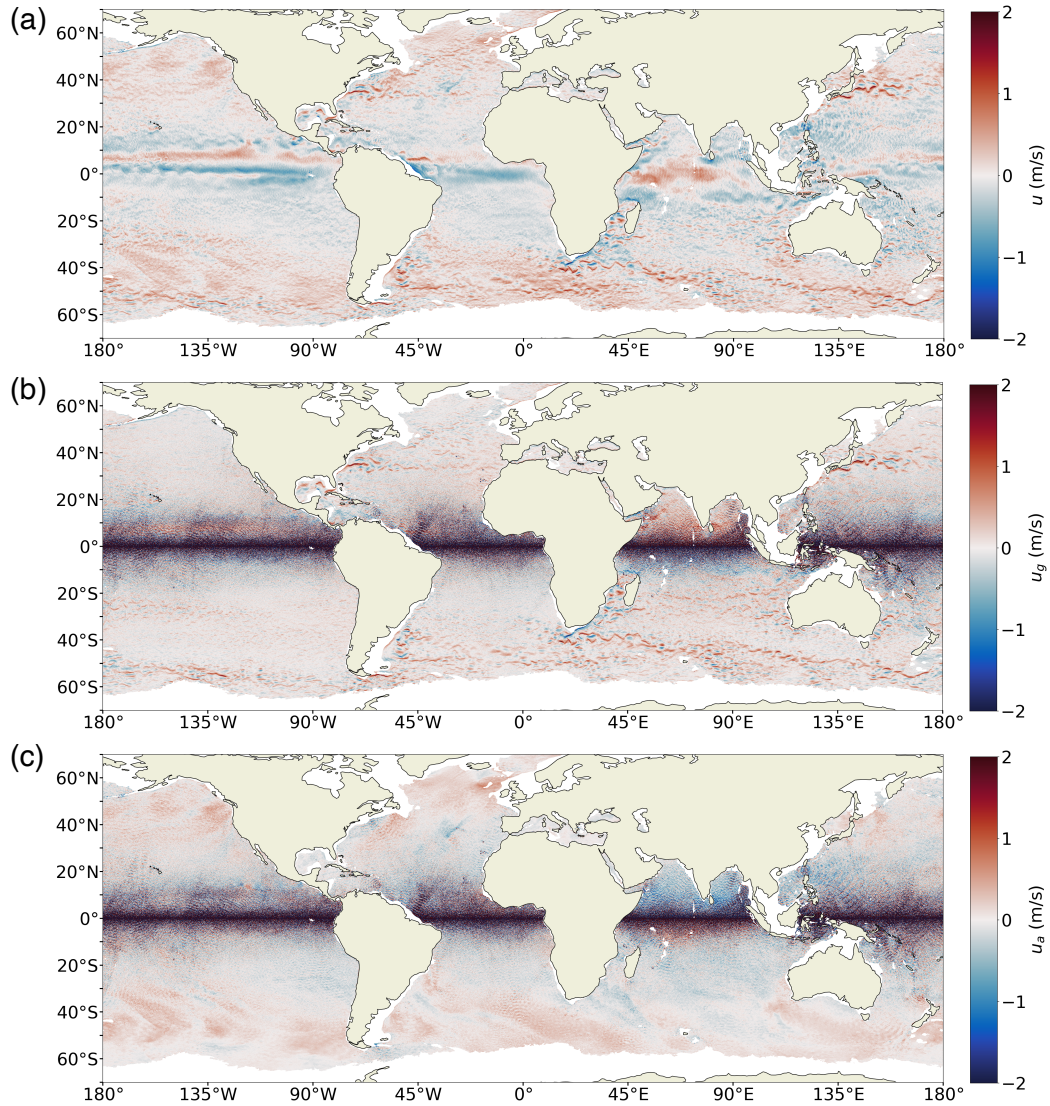
- 501 Large, W. G., McWilliams, J. C., & Doney, S. C. (1994). Oceanic vertical mixing - a review
502 and a model with a nonlocal boundary-layer parameterization. *Reviews of Geophysics*,
503 *32*(4), 363-403.
- 504 Lévy, M., Franks, P. J. S., & Smith, K. S. (2018). The role of submesoscale currents in
505 structuring marine ecosystems. *Nature Communications*, *9*, 4758.
- 506 Lumpkin, R., & Johnson, G. C. (2013). Global ocean surface velocities from drifters:
507 Mean, variance, el nino-southern oscillation response, and seasonal cycle. *Journal of*
508 *Geophysical Research-Oceans*, *118*(6), 2992-3006.
- 509 Marshall, J., Adcroft, A., Hill, C., Perelman, L., & Heisey, C. (1997). A finite-volume,
510 incompressible navier stokes model for studies of the ocean on parallel computers.
511 *Journal of Geophysical Research: Oceans*, *102*(C3), 5753-5766.
- 512 McWilliams, J. C. (2016). Submesoscale currents in the ocean. *Proceedings of the Royal*
513 *Society a-Mathematical Physical and Engineering Sciences*, *472*(2189).
- 514 Morrow, R., Fu, L. L., Arduin, F., Benkiran, M., Chapron, B., Cosme, E., . . . Zaron, E. D.
515 (2019). Global observations of fine-scale ocean surface topography with the surface
516 water and ocean topography (swot) mission. *Frontiers in Marine Science*, *6*, 232.
- 517 Morrow, R., & Le Traon, P. Y. (2012). Recent advances in observing mesoscale ocean
518 dynamics with satellite altimetry. *Advances in Space Research*, *50*(8), 1062-1076.
- 519 Nelson, A. D., Arbic, B. K., Menemenlis, D., Peltier, W. R., Alford, M. H., Grisouard, N.,
520 & Klymak, J. M. (2020, May). Improved Internal Wave Spectral Continuum in a
521 Regional Ocean Model. *Journal of Geophysical Research: Oceans*, *125*(5).
- 522 Penven, P., Halo, I., Pous, S., & Marié, L. (2014). Cyclogeostrophic balance in the mozam-
523 bique channel. *Journal of Geophysical Research: Oceans*, *119*(2), 1054-1067.
- 524 Ponte, A. L., Klein, P., Dunphy, M., & Le Gentil, S. (2017). Low-mode internal tides and
525 balanced dynamics disentanglement in altimetric observations: Synergy with surface
526 density observations. *Journal of Geophysical Research-Oceans*, *122*(3), 2143-2155.
- 527 Qiu, B., Chen, S., Klein, P., Wang, J., Torres, H., Fu, L.-L., & Menemenlis, D. (2018).
528 Seasonality in transition scale from balanced to unbalanced motions in the world
529 ocean. *Journal of Physical Oceanography*, *48*(3), 591-605.
- 530 Rimac, A., von Storch, J. S., Eden, C., & Haak, H. (2013). The influence of high-resolution
531 wind stress field on the power input to near-inertial motions in the ocean. *Geophysical*
532 *Research Letters*, *40*(18), 4882-4886.
- 533 Rio, M.-H. (2003). High-frequency response of wind-driven currents measured by drifting
534 buoys and altimetry over the world ocean. *Journal of Geophysical Research*, *108*,
535 3283.
- 536 Rocha, C. B., Chereskin, T. K., Gille, S. T., & Menemenlis, D. (2016). Mesoscale to sub-
537 mesoscale wavenumber spectra in drake passage. *Journal of Physical Oceanography*,
538 *46*(2), 601-620.
- 539 Rodriguez, E., Wineteer, A., Perkovic-Martin, D., Gal, T., Stiles, B. W., Niamsuwan, N.,
540 & Monje, R. R. (2018). Estimating ocean vector winds and currents using a ka-band
541 pencil-beam doppler scatterometer. *Remote Sensing*, *10*(4).
- 542 Savage, A. C., Arbic, B. K., Richman, J. G., Shriver, J. F., Alford, M. H., Buijsman, M. C.,
543 . . . Zamudio, L. (2017). Frequency content of sea surface height variability from
544 internal gravity waves to mesoscale eddies. *Journal of Geophysical Research-Oceans*,
545 *122*(3), 2519-2538.
- 546 Schubert, R., Gula, J., Greatbatch, R. J., Baschek, B., & Biastoch, A. (2020). The Submes-
547 oscale Kinetic Energy Cascade: Mesoscale Absorption of Submesoscale Mixed Layer
548 Eddies and Frontal Downscale Fluxes. *Journal of Physical Oceanography*, *50*(9), 2573-
549 2589.
- 550 Shrira, V. I., & Almelah, R. B. (2020). Upper-ocean Ekman current dynamics: a new
551 perspective. *Journal of Fluid Mechanics*, *887*, A24.
- 552 Siegelman, L., Klein, P., Rivière, P., Thompson, A. F., Torres, H. S., Flexas, M., & Men-
553 emenlis, D. (2020). Enhanced upward heat transport at deep submesoscale ocean
554 fronts. *Nature Geoscience*, *13*(1), 50-55.
- 555 Su, Z., Torres, H., Klein, P., Thompson, A. F., Siegelman, L., Wang, J., . . . Hill, C. (2020).

- 556 High-frequency submesoscale motions enhance the upward vertical heat transport in
557 the global ocean. *Journal of Geophysical Research: Oceans*, 125(9), e2020JC016544.
- 558 Su, Z., Wang, J., Klein, P., Thompson, A. F., & Menemenlis, D. (2018). Ocean subme-
559 soscales as a key component of the global heat budget. *Nature communications*, 9(1),
560 775.
- 561 Thomas, L. N., Tandon, A., & Mahadevan, A. (2008). Submesoscale processes and dynamics.
562 In *Ocean modeling in an eddying regime* (p. 17-38). American Geophysical Union.
- 563 Torres, H. S., Klein, P., Menemenlis, D., Qiu, B., Su, Z., Wang, J. B., ... Fu, L. L.
564 (2018). Partitioning ocean motions into balanced motions and internal gravity waves:
565 A modeling study in anticipation of future space missions. *Journal of Geophysical*
566 *Research-Oceans*, 123(11), 8084-8105.
- 567 Vallis, G. (2007). Atmospheric and oceanic fluid dynamics: Fundamentals and large-scale
568 circulation. *Cambridge University Press*, 745 pp.
- 569 Wang, J., Fu, L. L., Torres, H. S., Chen, S. M., Qiu, B., & Menemenlis, D. (2019). On the
570 spatial scales to be resolved by the surface water and ocean topography ka-band radar
571 interferometer. *Journal of Atmospheric and Oceanic Technology*, 36(1), 87-99.
- 572 Wang, W., & Huang, R. X. (2004). Wind energy input to the ekman layer. *Journal of*
573 *Physical Oceanography*, 34(5), 1267-1275.
- 574 Yu, X., Naveira Garabato, A. C., Martin, A. P., & Marshall, D. P. (2021). The annual cycle
575 of upper-ocean potential vorticity and its relationship to submesoscale instabilities.
576 *Journal of Physical Oceanography*, 51(2), 385-402.
- 577 Yu, X., Ponte, A. L., Elipot, S., Menemenlis, D., Zaron, E. D., & Abernathey, R. (2019).
578 Surface kinetic energy distributions in the global oceans from a high-resolution nu-
579 merical model and surface drifter observations. *Geophysical Research Letters*, 46(16),
580 9757-9766.



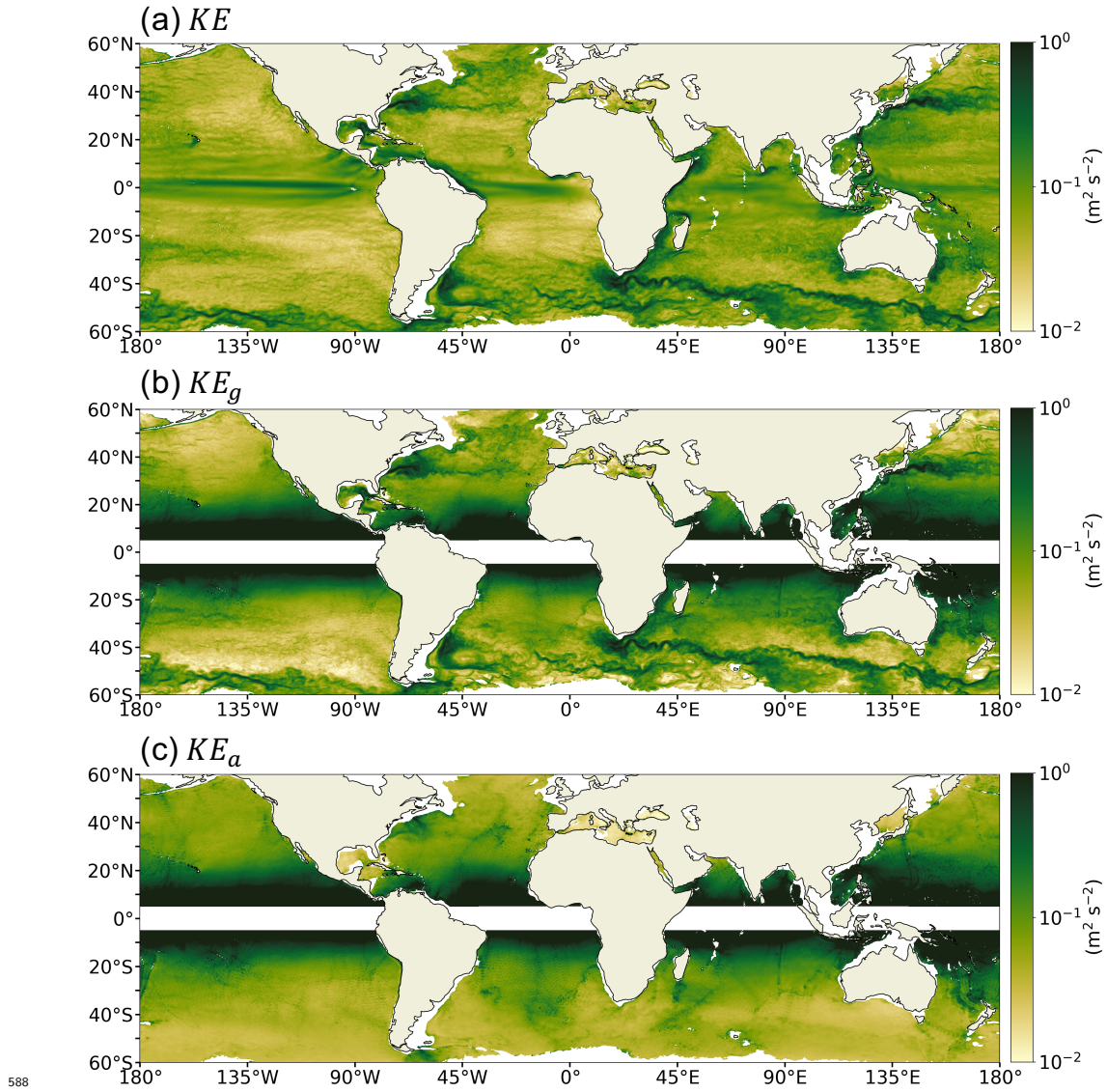
581

582 **Figure 1.** Snapshot of the sea surface height at 08:00 on 24 November 2011 from the LLC4320
583 simulation.



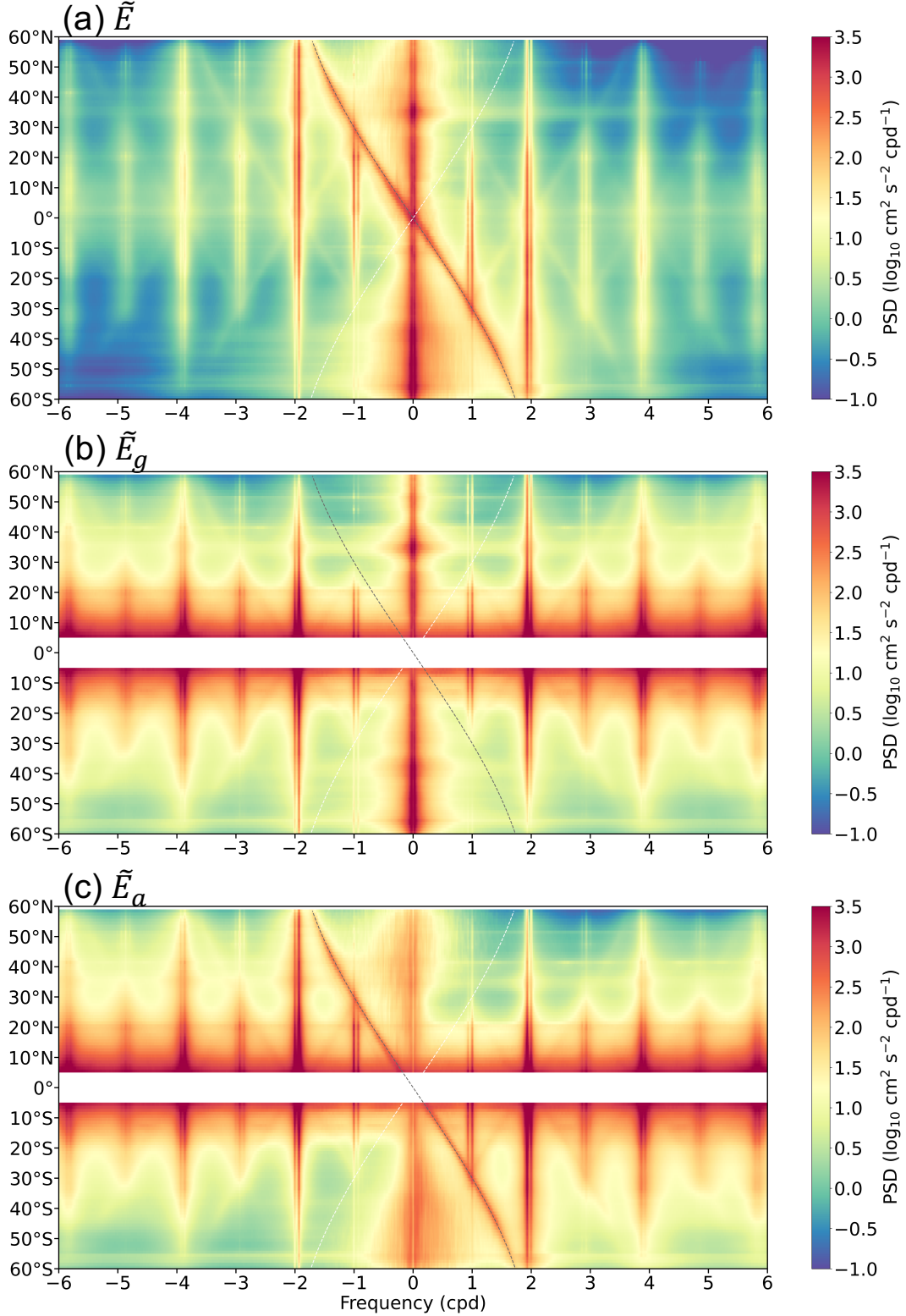
584

585 **Figure 2.** Snapshot of (a) the surface zonal velocity, (b) the zonal component of geostrophically
 586 computed velocity, and (c) the zonal component of ageostrophic velocity at 08:00 on 24 November
 587 2011 from the LLC4320 simulation. The coastal and ice-covered regions are excluded.



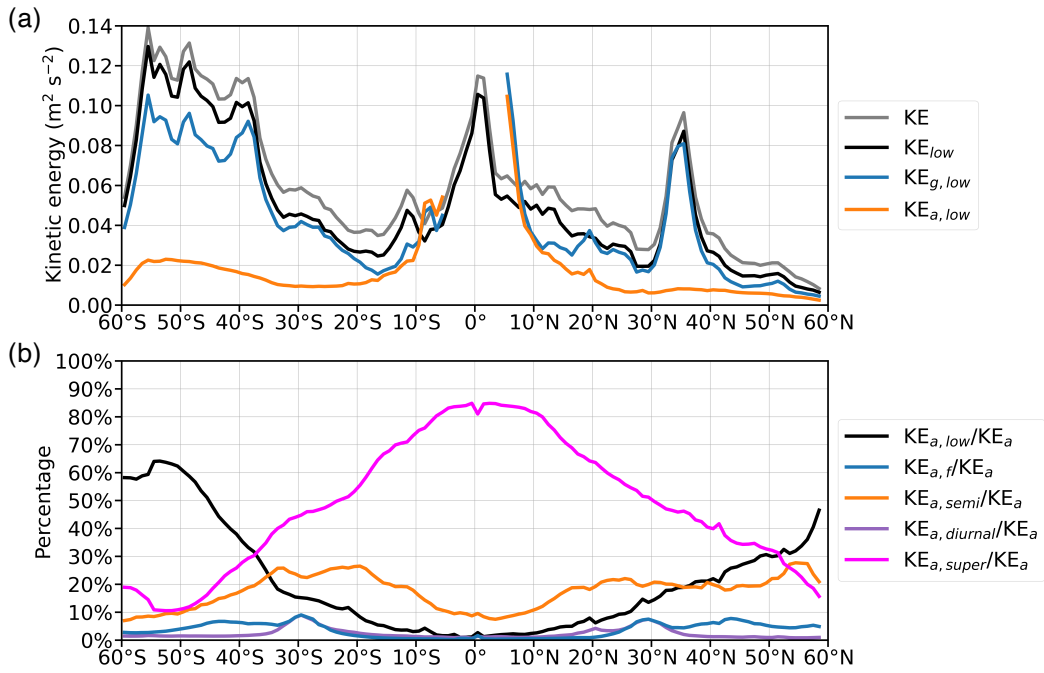
588

589 **Figure 3.** Global distributions of annually averaged (a) total, (b) geostrophically computed and
 590 (c) ageostrophic kinetic energies at the ocean surface from the LLC4320 simulation.



591

592 **Figure 4.** Zonally averaged rotary frequency spectra in 1° latitude bins from (a) total, (b)
 593 geostrophically computed and (c) ageostrophic velocity fields at the surface layer of the LLC4320
 594 simulation. The inertial frequency ($-f/2\pi$ cpd) is indicated by the gray dashed line and the Coriolis
 595 frequency ($f/2\pi$ cpd) is indicated by the white dashed line.



596

597

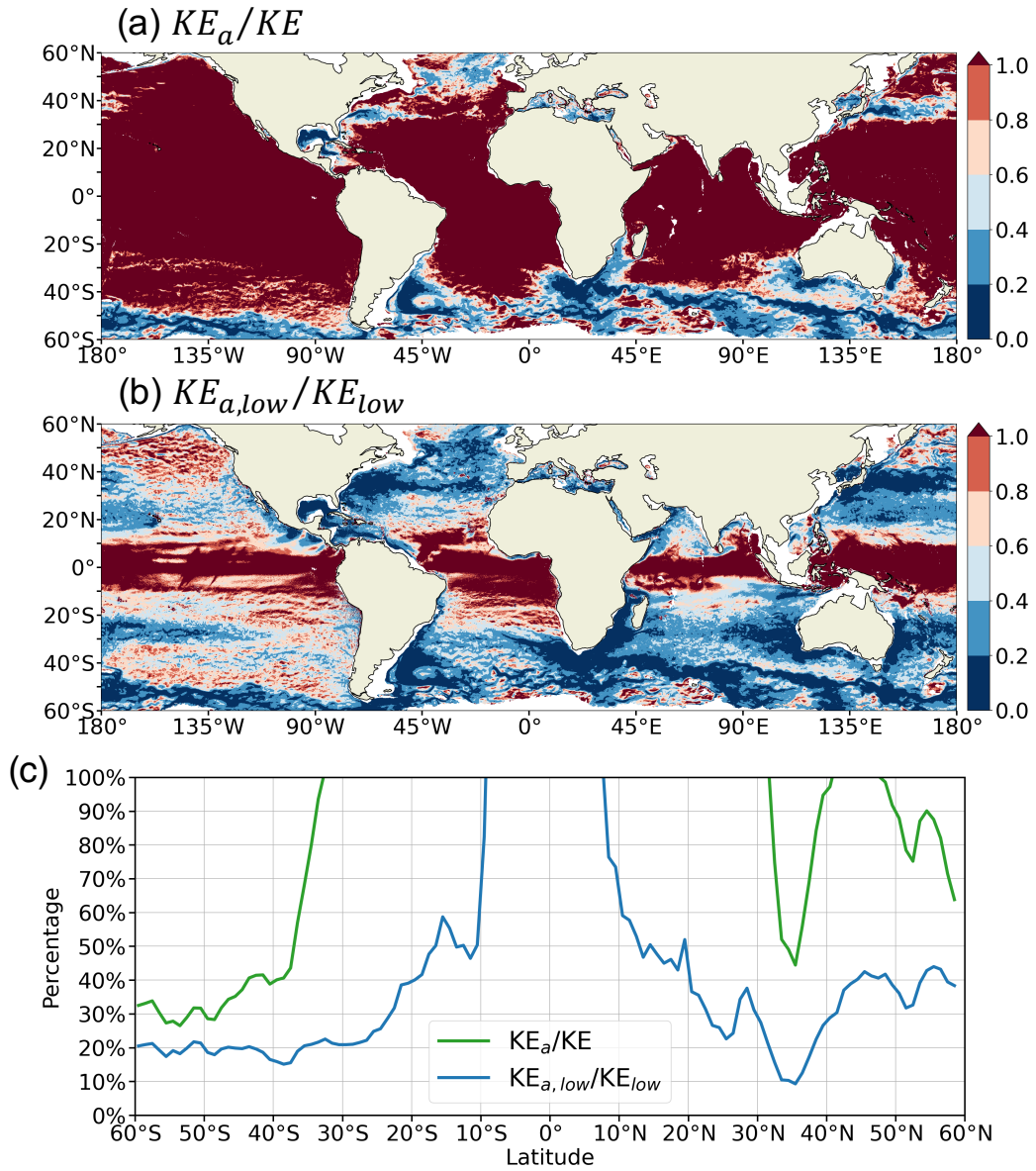
598

599

600

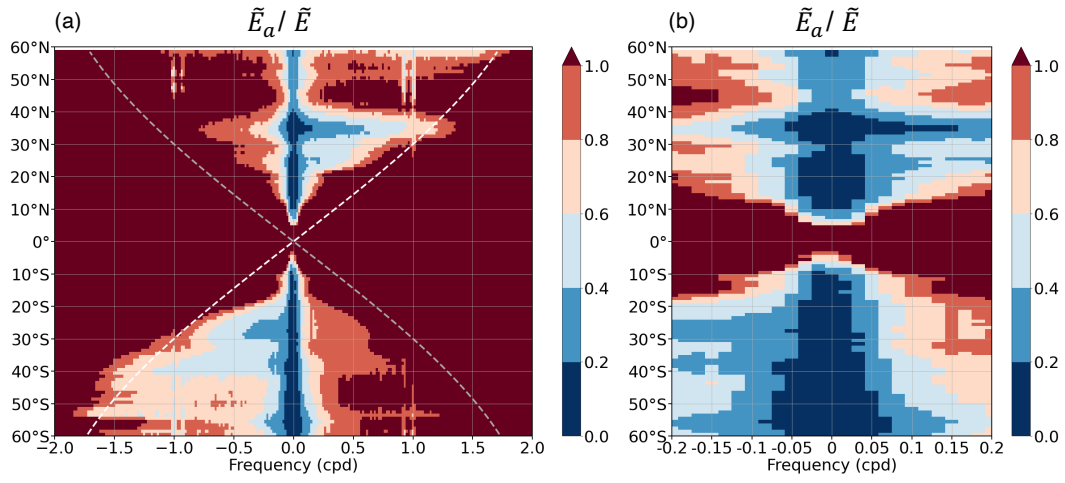
601

Figure 5. (a) Comparison of the zonally-averaged total kinetic energy (gray), and low-frequency component of total (black), geostrophically computed (blue) and ageostrophic (orange) kinetic energies in 1° latitude bins. (b) Percentage of low-frequency (black), near-inertial (blue), semidiurnal (orange), diurnal (purple) and supertidal (magenta) kinetic energies to the ageostrophic kinetic energy in 1° latitude bins.



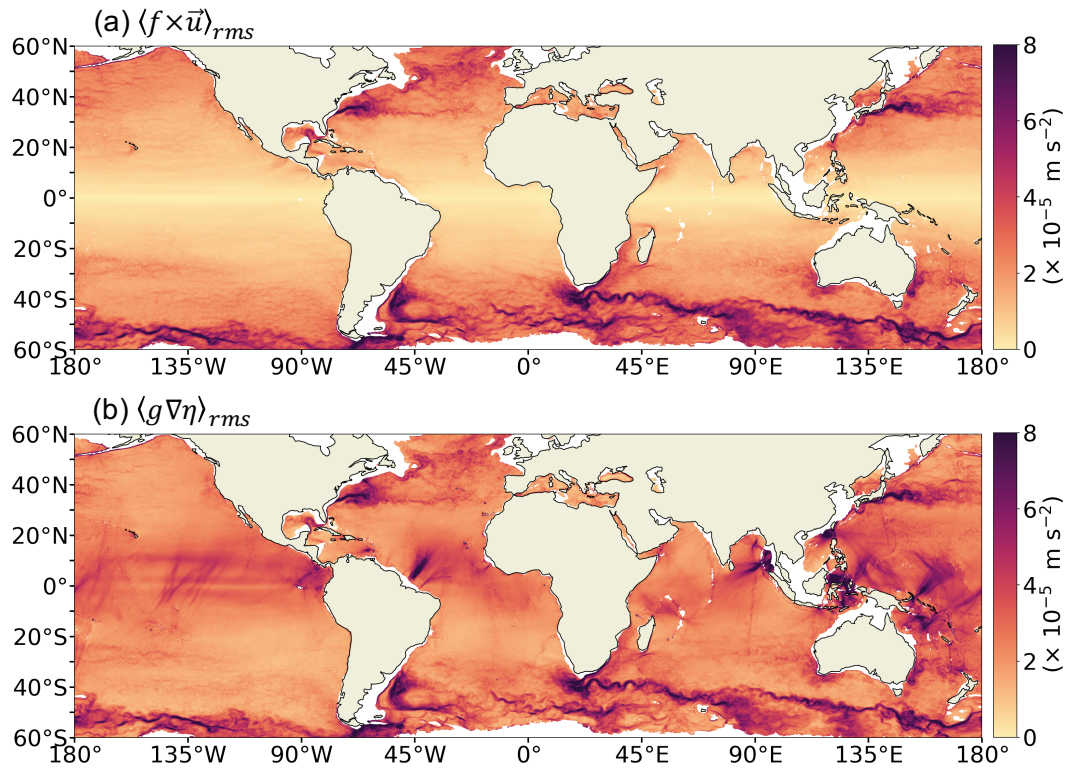
602

603 **Figure 6.** (a) Global map of the ratio between ageostrophic kinetic energy KE_a and total
 604 kinetic energy KE . (b) Global map of the ratio between low-frequency ageostrophic kinetic energy
 605 $KE_{a,low}$ and low-frequency total kinetic energy KE_{low} . (c) Zonally averaged KE_a/KE (green)
 606 and $KE_{a,low}/KE_{low}$ (blue) in 1° latitude bins.



607

608 **Figure 7.** (a) The ratio of zonally averaged rotary frequency spectra from the ageostrophic
 609 velocity field and the total velocity field, \tilde{E}_a/\tilde{E} , at the surface layer of the LLC4320 simulation in
 610 1° latitude bins. The inertial frequency ($-f/2\pi$ cpd) is indicated by the gray dashed line and the
 611 Coriolis frequency ($f/2\pi$ cpd) is indicated by the white dashed line. (b) Same as (a) but zoomed
 612 in over the frequency range between -0.2 cpd and 0.2 cpd.

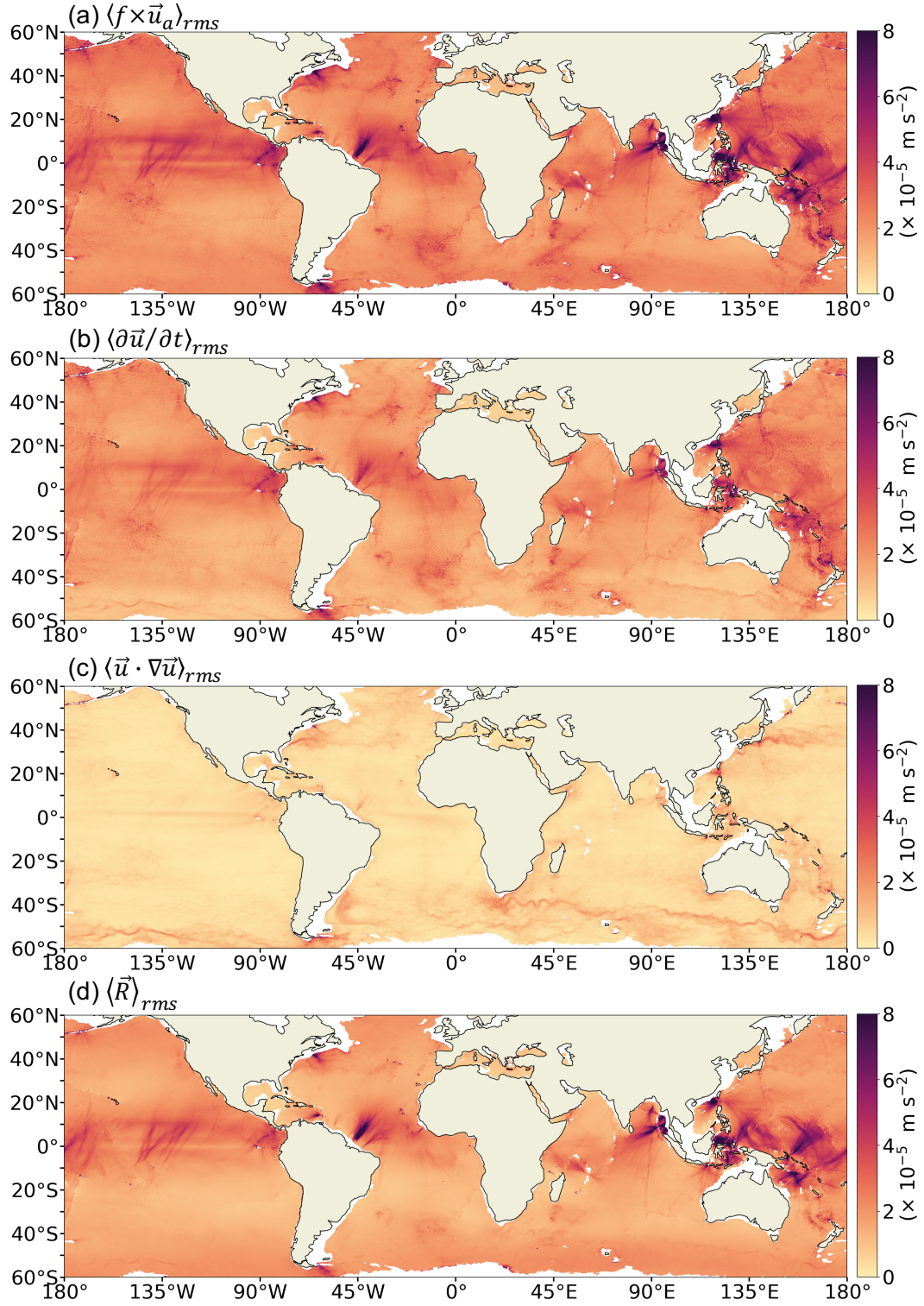


613

614

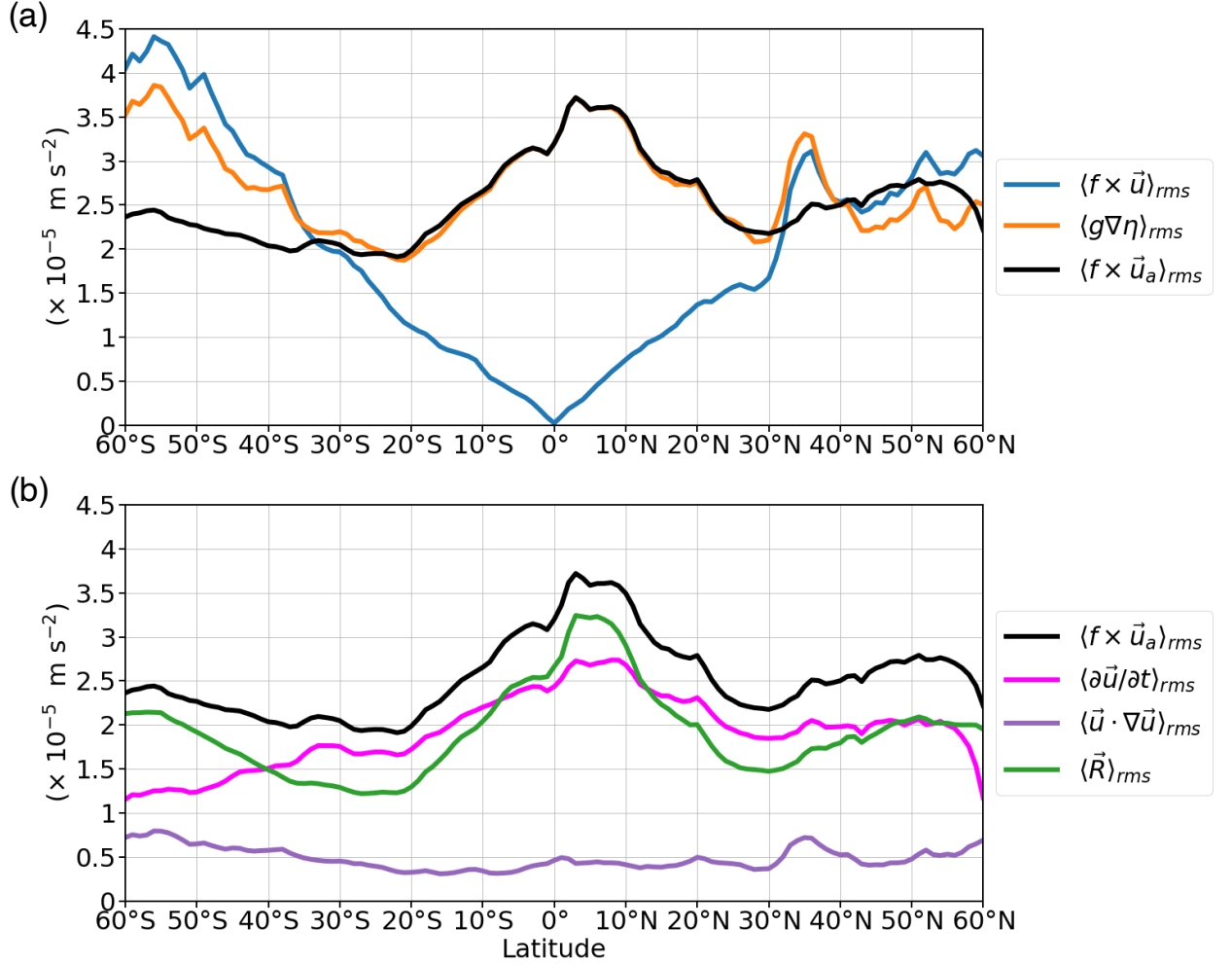
615

Figure 8. Global distributions of the root-mean-square values of (a) the linear Coriolis term $\langle f \times \vec{u} \rangle_{rms}$ and (b) the pressure gradient term $\langle g \nabla \eta \rangle_{rms}$.



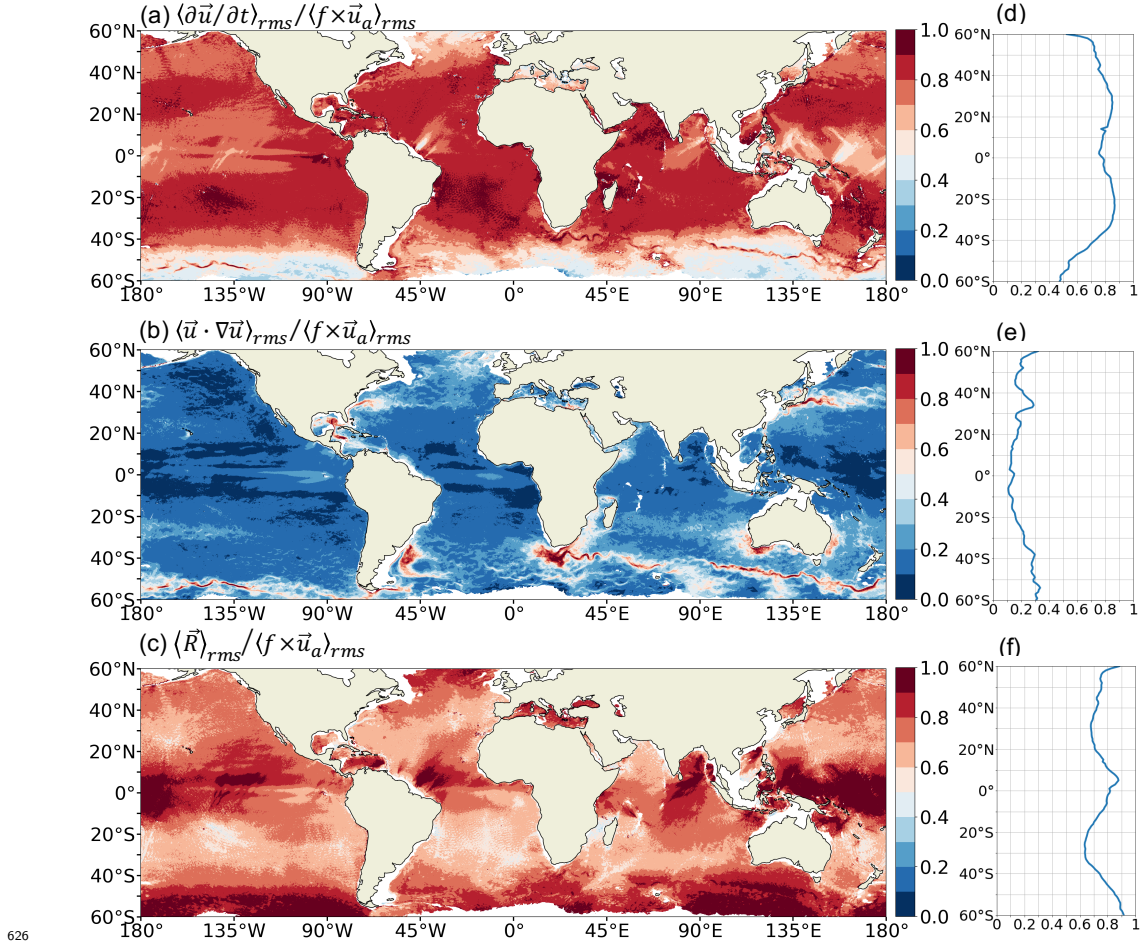
616

617 **Figure 9.** Global distributions of the root-mean-square values of (a) the ageostrophic Coriolis
 618 term $\langle f \times \vec{u}_a \rangle_{rms}$, (b) the time acceleration term $\langle \partial \vec{u} / \partial t \rangle_{rms}$, (c) the nonlinear advection term
 619 $\langle \vec{u} \cdot \nabla \vec{u} \rangle_{rms}$ and (d) the residual term $\langle \vec{R} \rangle_{rms}$.



620

621 **Figure 10.** (a) Zonally averaged root-mean-square values of the linear Coriolis term ($\langle f \times$
 622 $\vec{u} \rangle_{rms}$, blue), the pressure gradient term ($\langle g \nabla \eta \rangle_{rms}$, orange) and the ageostrophic Coriolis term
 623 ($\langle f \times \vec{u}_a \rangle_{rms}$, black). (b) Same as (a) but for the time acceleration term ($\langle \partial \vec{u} / \partial t \rangle_{rms}$, magenta),
 624 the advection term ($\langle \vec{u} \cdot \nabla \vec{u} \rangle_{rms}$, purple) and the residual term ($\langle \vec{R} \rangle_{rms}$, green). The ageostrophic
 625 Coriolis term ($\langle f \times \vec{u}_a \rangle_{rms}$, black) is also shown as a reference.



626

627 **Figure 11.** Fraction of each term to the ageostrophic Coriolis term. Global maps of the ratio of
 628 (a) the time acceleration term over the ageostrophic Coriolis term $\langle \partial \vec{u} / \partial t \rangle_{rms} / \langle f \times \vec{u}_a \rangle_{rms}$, (b) the
 629 advection term over the ageostrophic Coriolis term $\langle \vec{u} \cdot \nabla \vec{u} \rangle_{rms} / \langle f \times \vec{u}_a \rangle_{rms}$ and (c) the residual
 630 term over the ageostrophic Coriolis term $\langle \vec{R} \rangle_{rms} / \langle f \times \vec{u}_a \rangle_{rms}$. Their zonal averages are shown in
 631 (d-f).